Communications in Computational Chemistry
Commun. Comput. Chem., Vol. 7, No. 3, 190–201
doi: 10.4208/cicc.2025.133.01
Regular Article

Computational Investigation into the Enzyme-Catalyzed [4+2] Cycloaddition of Decatromicin

Wenhao Gu[1] and John Z. H. Zhang[1,2,3,4,*]

[1]*School of Chemistry and Molecular Engineering, East China Normal University at Shanghai, 200062, China*;

[2]*Faculty of Synthetic Biology, Shenzhen University of Advanced Technology, Shenzhen 518107, China*;

[3]*NYU-ECNU Center for Computational Chemistry and Shanghai Frontiers Science Center of AI and DL, NYU Shanghai, Shanghai 200126, China*;

[4]*Department of Chemistry, New York University, NY, NY10003, USA.*

[*] Corresponding author: John.zhang@nyu.edu

Received on 13 May 2025; Accepted on 3 June 2025

Abstract: This study presents a detailed examination of enzyme-catalyzed pericyclic reactions, specifically focusing on the synthesis of spirotetronate (decatromicin), catalyzed by the Plol4 enzyme. Utilizing the QM/MM method, we have discovered that the Plol4 enzyme significantly reduces the energy barrier in the Diels-Alder (DA) reaction, demonstrating its effectiveness in facilitating complex chemical processes. Our analysis suggests that this reduction is partly due to the interaction between the substrate and active site residues within the enzyme, which prearranges the substrate in a manner conducive to the [4+2] cycloaddition. Moreover, we observed a notable shift in the DA reaction mechanism from a concerted approach within the gas phase to an asynchronous approach within the enzymatic environment. This finding highlights the unique role of Plol4 in altering reaction pathways and underscores the enzyme's potential in synthetic applications. Overall, this research provides valuable insights into the mechanisms of enzyme-catalyzed reactions and their implications for the synthesis of polycyclic compounds.

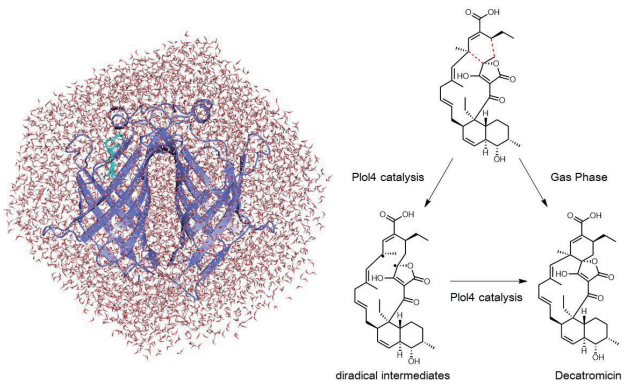

Key words: Enzyme, Cycloaddition, Decatromicin, QM/MM, Diels-Alder, reaction pathways, synthesis.

1. Introduction

For almost a hundred years, the Diels-Alder reaction has been a key method for synthetic chemists in creating both important natural substances and their non-natural counterparts, which hold biological importance. This reaction is particularly useful for constructing cyclic products with excellent region and stereoselectivity, and thus is considered one of the most important reactions in organic synthesis. Over the past decade, numerous research groups have applied enzymes capable of catalyzing the Diels-Alder reaction to the biosynthesis of natural products [1-16]. Spirotetronate compounds, known for their anticancer and antimicrobial properties, hold potential as pharmaceutical agents. Consequently, many research groups have dedicated significant efforts in recent years to the synthesis and identification of these substances. One of the hottest areas of research is the biosynthesis of spirotetronates. In recent years, enzymes capable of catalyzing the synthesis of spirotetronates have been successively reported, marking a notable advancement in the field.

In 2020, the Liu Wen research group collaborated with the Houk research team to investigate the activation and stereoselective mechanism of the intramolecular Diels-Alder reaction catalyzed by the monofunctional D-A enzyme PyrI4 [17]. This enzyme plays a pivotal role in the biosynthesis of pyrroindomycins, an important natural product within the Spirotetronates family, particularly in the formation of its critical spiro-tetronate backbone. The key activation effects of PyrI4 stem primarily from acid catalysis, an induced-fit conformational adaptation mechanism, and its unique "lid-closing" feature that stabilizes the Diels-Alder reaction transition state. Additionally, PyrI4 enzyme enhances the intrinsic Diels-Alder stereoselectivity of the substrate, leading to the stereoselective synthesis of the product.

In the subsequent year of 2022, their investigations utilizing quantum mechanics and molecular dynamics demonstrated the distinct operational modes of the PyrE3 enzyme in catalyzing the biosynthesis of pyrroindomycins [18]. This enzyme adeptly arranges anionic polyene substrates into a high-energy reaction conformation. Within this conformation, an inverse electron demand Diels-Alder reaction can occur with a low energy barrier. The stereoselectivity is achieved through strong binding interactions within the endo stereochemical arrangement and local spatial constraints imposed on the endo-1, 3-diene unit. These findings elucidate the divergent mechanisms of PyrE3 and PyrI4, highlighting nature's evolutionary prowess in developing multiple methods to catalyze Diels-Alder reactions.

In 2023, Liu Wen, Pan Lifeng, and Ken N. Houk collaborated once again, and their research teams made a groundbreaking discovery in the biosynthetic pathway of pyrroindomycin: a novel cyclase enzyme responsible for the formation of chiral spiro-rings [19]. This enzyme, characterized by a β-barrel fold, operates independently of light activation. When used with pyrroindomycin intermediates as substrates, it not only produces exo and endo [4+2] addition products but also generates exo [2+2] addition products. Employing structural biology and computational chemistry, the authors elucidated the molecular mechanisms through which this enzyme catalyzes different cycloaddition reactions, achieving region- and stereoselectivity control. They proposed and validated a reaction process involving bi-radical intermediates, which thermodynamically favors [4+2] products and kinetically favors [2+2] products. Through directed evolution, the researchers precisely modulated the chemical and stereoselectivity of the enzyme, obtaining mutant proteins that exclusively catalyze single cycloaddition reactions of exo [4+2], endo [4+2], and exo [2+2].

However, another significant compound in the Spirotetronates family[20-30], decatromicin, has not been extensively reported in terms of its biosynthesis. Compared to pyrroindomycins,decatromicin possesses two additional carbon atoms in its main carbon chain. The Liu Wen research group hypothesized that the enzyme Plol4 might catalyze the synthesis of decatromicin-like substances [19]. In 2022, Yoganathan Kanagasundaram, Veronica W. Ng, Siew-Bee Ng, and others identified several previously unreported Spirotetronate compounds from extracts of Actimonadura sp [31]. They evaluated their antibacterial activities against Gram-negative bacteria, including Acinetobacter baumannii, and Gram-positive bacteria, such as Staphylococcus aureus. Additionally, they studied their cytotoxic effects on human cancer A549 cells. Among these, decatromicin D showed promising results in these aspects. Consequently, we decided to investigate whether the Plol4 enzyme catalyzes the synthesis of decatromicin D through advanced computational methods, including Density Functional Theory (DFT) calculations and Quantum Mechanics/Molecular Mechanics Molecular Dynamics (QM/MM MD) simulations. This approach reflects a sophisticated blend of experimental and computational strategies to unravel the intricate enzymatic pathways involved in the natural synthesis of complex molecular structures.

2. Computational details

2.1 DFT calculations

Gaussian16 was used for all density functional theory computations [32]. Geometry optimization and subsequent frequency calculations were conducted for each species at the B3LYP/6-31G(d) level of theory, incorporating Grimme's D3 empirical dispersion correction [33-34], in the gas phase and utilizing an ultrafine level integration grid. Analysis of normal vibrational modes ensured that the optimized structures were either minima or transition states. Zero-point vibrational energy (ZPE) and thermal corrections were determined using B3LYP/6-31G(d)-D3 frequencies. The potential energy of each structure was calculated at the B3LYP/6-31G(d)-D3 level. Gibbs free energies reported at 298K were the sum of these single-point electronic energies, ZPE, and thermal corrections, all determined using B3LYP/6-31G(d)-D3 frequencies and an ultrafine level integration grid.

2.2 Docking calculations

Autodock Vina[35] was employed for docking calculations. The docking target was Chain A of the crystal structure of Diels-Alderase Plol4 (PDB: 7X7Z). Any substrate present in the crystal structure was removed. We centered a 16Å×16Å×16Å grid box on the catalytic site. The DFT- optimized structure of each substrate, specifically the optimized transition state in the gas phase, was docked into the binding site. For docking the transition state, we used a rigid docking approach, meaning no bonds were allowed to rotate. The docking pose with the lowest energy was selected, reported, and utilized for further investigations..

2.3 Classical molecular dynamics simulations

Molecular dynamics (MD) simulations utilized the Amber 20 program and AmberTools 20 packages [36]. For MD simulations involving proteins and substrates, we used structures from docking calculations (Chain A, Chain B, and the transition state structure). The protonation states of each protein were determined using the PDB2PQR Server with PROPKA at pH 7.3. Explicit water MD simulations were conducted using the GPU-accelerated pmemd code. The protein scaffold employed an evolved version of the Stony Brook modification of the Amber 99 force field (ff14SB). SPCE parameters were assigned to water molecules. Ligand partial charges were fitted to the electrostatic potential generated at the HF/6-31G(d) level using the restrained electrostatic potential (RESP) model, calculated via the Merz-Singh-Kollman scheme in the Gaussian 16 program package. For simulations with a bound transition state, two bond-forming distances of the ligand were restrained to 2.0 Å and 3.4 Å, mirroring the QM-optimized transition state structure, using a harmonic constraint with a force constant of 200 kcal $mol^{-1}Å^{-2}$. No constraints were applied in simulations without a bound transition state. Each protein complex was placed in an octahedral box with a 10 Å buffer of SPCE water molecules, created using the leap module. Systems were neutralized with explicit Na+ counter ions. Long-range electrostatic effects were modeled using the particle mesh Ewald method under periodic boundary conditions.

The MD simulations were executed through the following stages: (1) Initial minimization was done for each system, with a cap of 100000 cycles, employing the steepest descent algorithm for the initial 50000 cycles. This was under constant volume (NVT) periodic boundary conditions, without the activation of the SHAKE algorithm. A positional restraint of 1000 kcal mol^{-1} $Å^{-2}$ was applied to the ligand, the backbone atoms (C and N), and the heavy atoms of the enzyme. (2)The ligand and enzyme's positional restraint was reduced to 200 kcal mol^{-1} $Å^{-2}$. This step involved a 1 ns heating process under constant volume (NVT) periodic boundary conditions, with the SHAKE algorithm activated to maintain the angle between hydrogen atoms fixed. The temperature was gradually increased from 0 K to 300 K over 900 ps using Langevin dynamics with a collision frequency of 2 ps^{-1}, followed by a 100 ps equilibrium process. (3) The positional restraint on the ligand and enzyme was further decreased to 100 kcal mol^{-1} $Å^{-2}$. This stage included a 2 ns equilibrium process under constant pressure (NPT) and a maintained temperature of 300 K, followed by a 1,000 ns production process under standard simulation conditions for constant pressure (NPT) and temperature. (4) The positional restraint on the enzyme was further decreased to 50 kcal mol^{-1} $Å^{-2}$. A 100 ns production process was then executed under standard simulation conditions of constant pressure (NPT) and a steady temperature of 300 K.

2.4 QM/MM/MD umbrella sampling

The QM/MM/MD calculations were conducted using the Amber 20 sander program. For the quantum mechanical (QM) portion, calculations were carried out using the ORCA program. These calculations focused on the substrate and some residues, using the B3LYP/6-31G(d) level of theoryand incorporating Grimme's D3 empirical dispersion correction. For the molecular mechanics (MM) part, the Stony Brook modification of the Amber 99 force field (ff14SB) parameters were employed for the other amino acid residues. The bond-forming distance was divided into several sampling windows. In each of these windows, a harmonic constraint was enforced with a force constant of 400 kcal mol−1Å−2, and the sampling was conducted over a period of 5 ps per window. To construct the potential of mean force diagram, the Weighted Histogram Analysis Method (WHAM) was utilized [37].

3. Results and discussion

3.1 DFT investigation of the uncatalyzed reaction

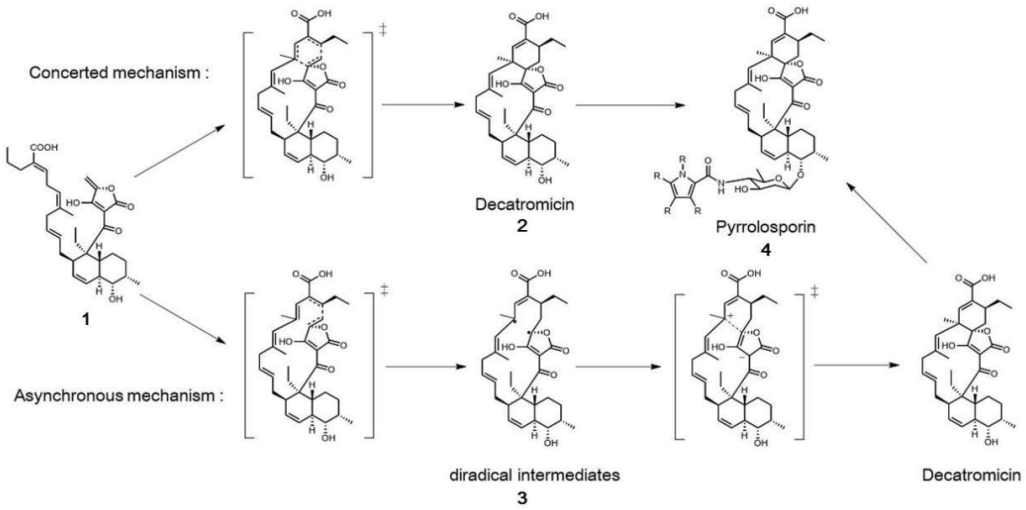

Scheme 1. Proposed cycloaddition mechanism of decatromicin.

As shown in Scheme 1, the formation of the decatromicin spiralic acid segment is achieved through a Diels-Alder (DA) reaction, which we believe could proceed through two different mechanisms. The first possible mechanism is a concerted mechanism, where the reactants directly form the product through a six-membered ring transition state. The second potential mechanism involves the stepwise formation of the two bonds involved in the DA reaction. This process would begin with the formation of a radical when

the first bond is formed, followed by a zwitterionic transition state, leading to the corresponding product. To unveil the reactivity of the substrate, we initially studied the uncatalyzed DA reaction using Density Functional Theory (DFT) and the B3LYP method. As illustrated in Figure 1, depending on the relative position and orientation of the diene and the dienophile, the substrate's DA reaction can yield two stereoisomers (endo-addition and exo-addition). To investigate the catalytic mechanism of the substrate, we focused on studying two stereoselectively transitional state structures and the reaction barriers.

In the gas phase, the endo-Diels−Alder reaction of 1 into 2 via transition state TS1 has a high Gibbs free energy barrier of 23.2 kcal/mol. The transition state is highly asynchronous with the C4−C5 bond (2.0 Å) more fully formed than the C6−C15 bond (3.4 Å). For the exo-Diels−Alder reaction (TS2), we were surprised to find out that Gibbs free energy barrier is only 11.3 kcal/mol; compared with endo-Diels−Alder reaction, it is more likely to react spontaneously at room temperature. However, the mechanism of its

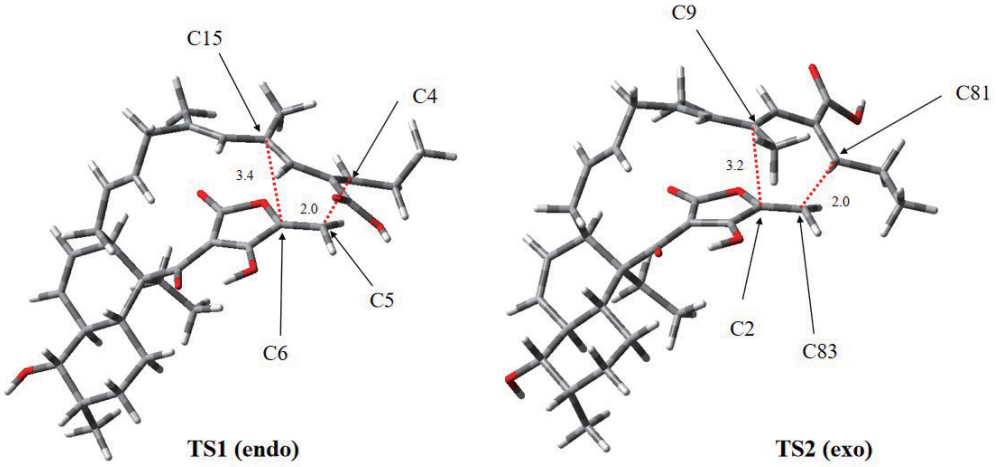

Figure 1. Transition-state geometry of TS1 and TS2; distances are in Å.

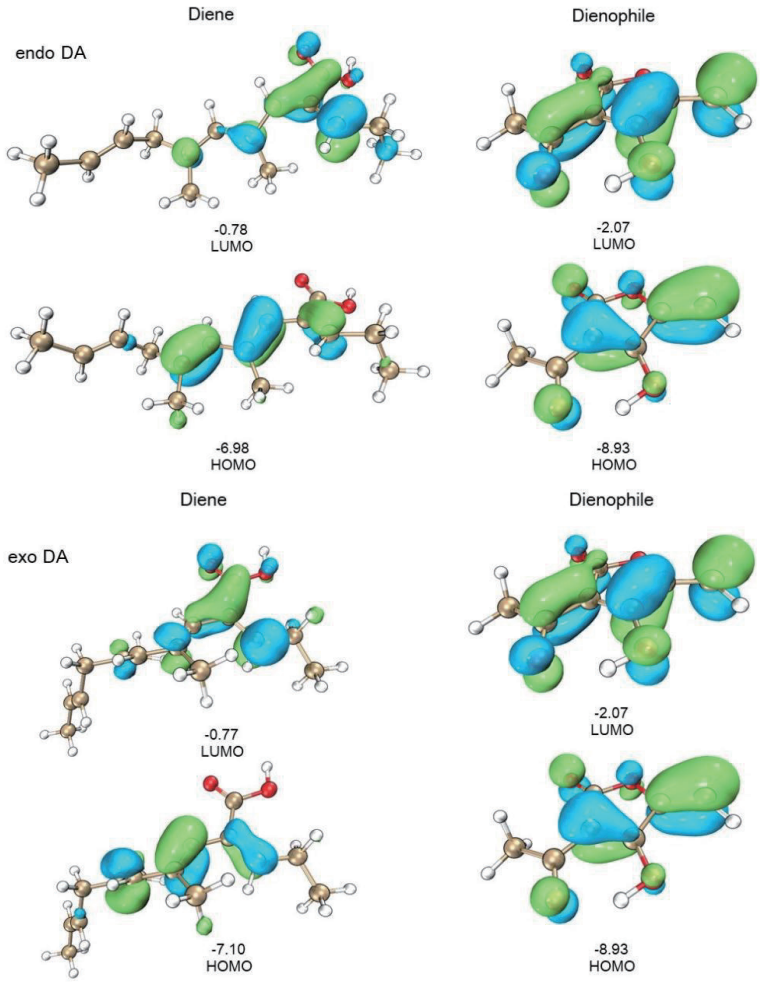

Figure 2. Orbital analysis for the diene and dienophile of endo-Diels−Alder reaction (top) and diene and dienophile of exo-Diels−Alder reaction (bottom).

reaction is still highly asynchronous with the C81−C83 bond (2.0 Å) more fully formed than the C2−C9 bond (3.2 Å). And IRC paths are shown in Figure S1 and Figure S2.

Through orbital analysis (Figure 2) we found that in the endo-Diels−Alder reaction of decatromicin, the gap between the HOMO of the dienophile and the LUMO of the diene (8.15 eV) is higher than the gap between the HOMO of the diene and the LUMO of the dienophile (4.91 eV), which indicates that reaction is an normal electron demand Diels−Alder reaction. Moreover, in the endo-Diels−Alder reaction of decatromicin, the gap between the HOMO of the dienophile and the LUMO of the diene (8.16 eV) is higher than the gap between the HOMO of the diene and the LUMO of the dienophile (5.03 eV). The difference between the two sets of HOMO−LUMO gap is not much.

3.2 MD simulations of substrate conformations

Decatromicin D is known to be derived from compound 1 through an endo-type Diels-Alder addition. However, based on the energy barrier calculations for the gas-phase Diels-Alder reaction, both endo and exo additions can spontaneously occur at room temperature. Nevertheless, due to the structural features of the Plol4 enzyme pocket, the stability of enzyme-substrate binding varies with the substrate conformation, potentially leading to conclusions different from those in the gas phase. Therefore, we have decided to perform classical molecular dynamics (MD) simulations for both types of stereoselective additions.

First, we used the two transition states, TS1 and TS2, optimized in the gas phase for stereoselective addition, as the initial substrates to perform molecular docking with the Plol4 enzyme (Figure 3). After obtaining two reasonable enzyme-substrate complex structures, we conducted classical molecular dynamics simulations on each for a duration of 100 ns. During the molecular dynamics simulations, ensuring the stability of the complex system is crucial for energy evaluation and exploring interaction mechanisms.

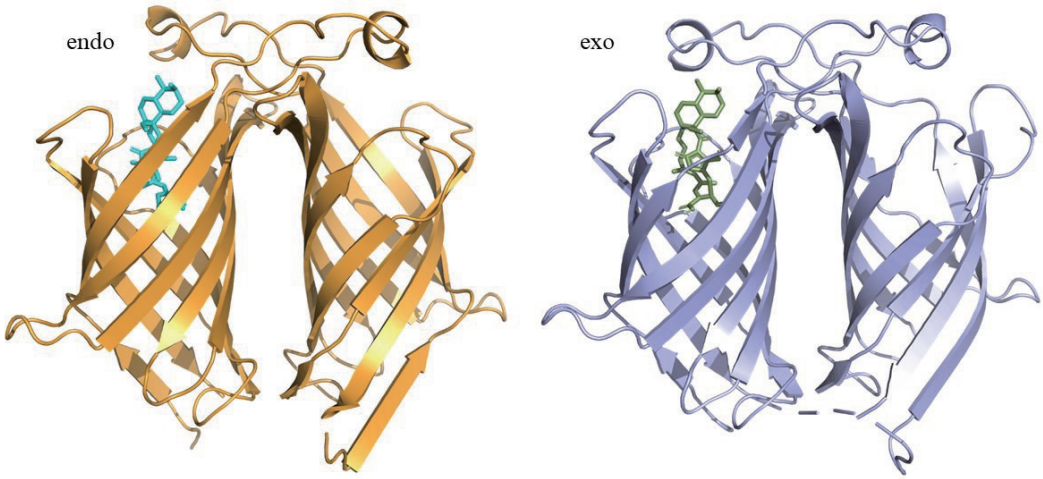

Figure 3. Structure of enzyme-substrate complex in endo and exo addition systems.

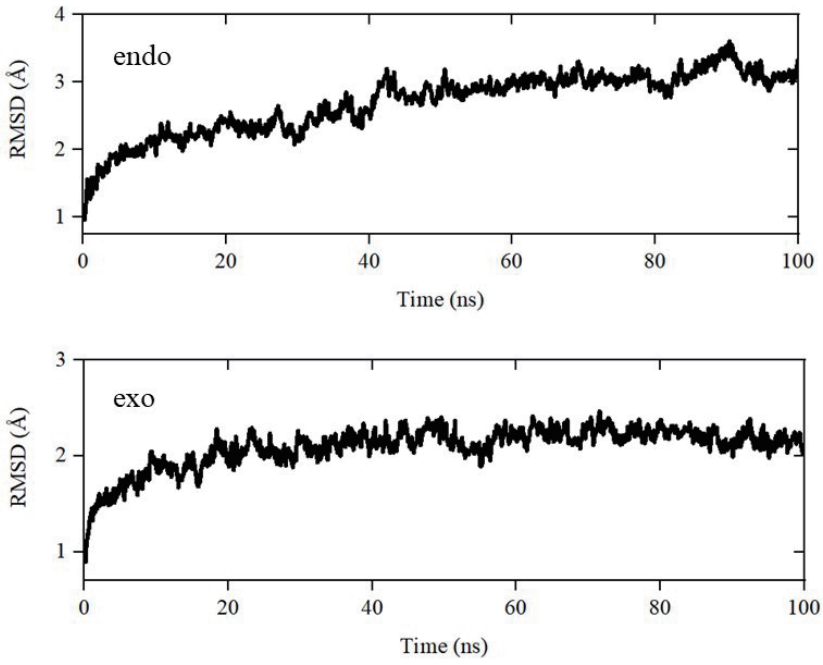

Figure 4. RMSD of endo and exo addition systems.

Root Mean Square Deviation (RMSD) is a key metric for assessing stability. Therefore, we calculated the RMSD for both the endo addition and exo addition systems, as shown in Figure 4. In the endo addition system, the overall RMSD stabilized at around 3.0 Å after 40 ns, with minor fluctuations near 90 ns. We checked several frames around 90 ns through simulation trajectories and found no abnormal structures. In the exo addition system, the overall RMSD stabilized at around 2.0 Å after 20 ns, with smaller fluctuations. Based on the above RMSD analysis, we consider both systems to have essentially reached equilibrium and are ready for further investigation.

3.3 Snapshot selection

The final frames from molecular dynamics trajectories were selected as QM/MM initial conformations. Hydrogen bond (HB) analysis around the substrate revealed key active-site residues (Figure 5), while the bi-cyclic region of decatromicin D was excluded from HB analysis due to its distance from reactive centers. Notably, the endo system exhibited four HBs (Y95-OH-O80, Q75-CO-H34, Q75-NH-O13, S135-OH-O10), whereas the exo system retained only two (Q75-NH-O8, S135-OH-O5). The absence of Y95 interaction in the exo system arises from substrate conformational changes displacing the diene carboxyl group from this residue..

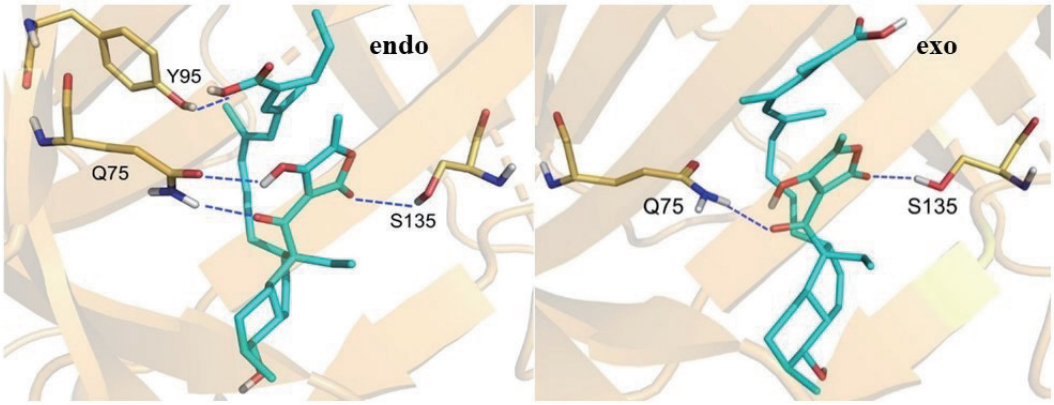

Figure 5. Hydrogen bonding of peripheral residues to substrates.

Although we have identified the residues that form hydrogen bonds with the substrate, we decided to further investigate the stability of these hydrogen bonds to ensure the accuracy of our results. We employed statistical analysis to compare the stability of hydrogen bonds by monitoring changes in bond lengths over the course of the simulation. As shown in Figure 6, we conducted separate analyses for both conformation systems.

The endo pathway exhibits distinct hydrogen bonding patterns: Q75 forms moderately stable interactions with H34 (HB1, avg 3.05 Å) and a less stable bond with O13 (HB2, avg 3.12 Å), where reduced stability likely facilitates product dissociation. Notably, Y95 establishes an exceptionally strong HB3 (avg 2.08 Å) with O80, while S135-O10 (HB4) displays transient elongations to 6 Å despite an average 2.79 Å bond length. In contrast, the exo system features a robust Q75-O8 interaction (HB5, avg 2.10 Å) but lacks Y95 participation due to substrate conformational shifts. Both pathways share analogous S135-mediated hydrogen bonds (HB4/HB6) showing intermittent 6 Å fluctuations (green/orange trajectories), though their average bond lengths remain below 3 Å (HB4: 2.79 Å; HB6: 2.05 Å).

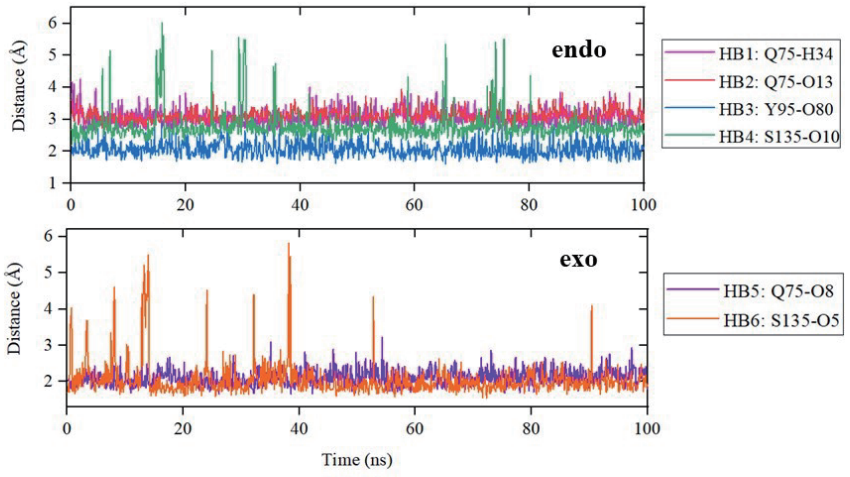

	HB1	HB2	HB3	HB4	HB5	HB6
Average (Å)	3.05	3.12	2.08	2.79	2.10	2.05
< 3.0 Å	48.2%	28.9%	99.9%	88.4%	99.8%	97.0%

Figure 6. Hydrogen bond length varies with simulation time.

Based on the results above, we have developed a clear plan for selecting residues in the QM region. For the endo addition system, HB1 and HB2 are relatively weak hydrogen bonds, and the atoms O13 and H34 connected by these bonds are far from the dienophile and are unlikely to influence the reaction; therefore, we will not include Q75 in the QM calculation region. HB3 is a very strong hydrogen bond, and the carboxyl group it connects is directly linked to the diene, making it necessary to include Y95 in the QM calculation region. For HB4, despite the abnormal range of bond length changes, the average bond length is a strong 2.79 Å. According to previous literature[17], when calculating other macrocyclic lactone antibiotics catalyzed by enzymes, the residue at this position is also included in the QM region; therefore, we will also include S135 in the QM calculation area.

For the exo addition system, although HB5 is a very strong hydrogen bond, it is still far from the dienophile, so it will not be included in the QM calculation region. Despite the unusual changes in the bond length of HB6, as mentioned above, we will include S135 in the QM calculation region for precautionary reasons.

3.4 NPA charge analysis

Table 1. Computed NPA charges of selected portions of the relevant species at the B3LYP-D3/6-31G* level[a].

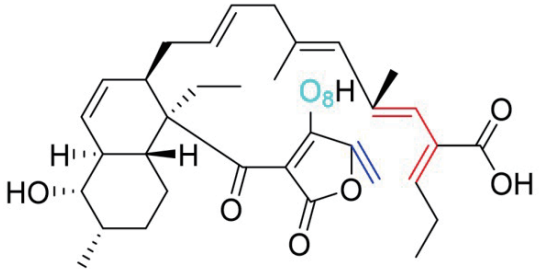

	Reactant	Reactant + enzyme	TS1	TS + enzyme
Diene moietye (endo)	-0.070	-0.017	-0.007	-0.008
Dienophile moiety (endo)	0.321	0.336	0.322	0.369
O8 (endo)	-0.649	-0.637	-0.663	-0.658
Diene moiety (exo)	-0.074	-0.097	-0.006	-0.010
Dienophile moiety (exo)	0.319	0.341	0.315	0.325
O59 (exo)	-0.655	-0.638	-0.677	-0.679

[a]The diene (red) and dienophile (blue) moieties are color-coded.

Hydrogen-bonding interactions in polar environments accelerate cycloadditions by modulating HOMO-LUMO gaps through electronic redistribution. Our NPA charge analysis (Table 1) reveals enzyme-induced polarization effects: in the endo pathway, the dienophile moiety exhibits enhanced positive charge within the enzyme environment (reactant: 0.336e vs gas-phase 0.321e; TS: 0.369e vs 0.322e), facilitated by substrate Q75-O8 hydrogen bonding that reduces O8's negative charge (-0.637e vs gas-phase -0.649e). Analogous polarization occurs in the exo system, where Q75-O59 interaction decreases O59's negativity (-0.638e vs -0.655e). Notably, enzyme-mediated charge modifications predominantly manifest in reactant states (diene: endo -0.017e vs gas -0.070e; exo -0.097e vs -0.074e), with TS charges converging between environments. These electronic perturbations lower dienophile electron density, synergizing with H-bond stabilization to reduce activation barriers.

3.5 Free energy simulations

After determining the QM calculation region in the previous section, to identify the minimum free energy paths for both the endo and exo additions and compare the free energy barriers of these potential paths within Plol4, we decided to perform free energy simulations. Due to practical reasons, all calculations in the QM region were conducted at the B3LYP-D3/6-31G(d) theoretical level.

We first performed umbrella sampling separately for the endo and exo addition systems. As shown in Figure 4-2, we defined the bonds between C4-C5 and C81-C83 as single reaction coordinates. From 1.4 Å to 4.5 Å, we set a window every 0.1 Å for umbrella sampling. Each window had a total simulation duration of 5 picoseconds, with sampling every 2 femtoseconds. We collected 2500 samples per window. After collection, the data were combined using Alan Grossfield's Weighted Histogram Analysis Method (WHAM) to produce the mean force potential, subsequently obtaining the distribution of free energy along the specific reaction coordinates.

As shown in the Figure 7, we displayed the potential of mean force (PMF) curves generated by setting a single reaction coordinate for both the endo and exo addition systems. Subsequently, we noticed anomalies in these results. In top picture of Figure 7, the reactants start from around 0 kcal/mol, overcoming a transition state barrier of about 16 kcal/mol, with the final product having a free energy of approximately 8 kcal/mol. This indicates that the products have higher energy compared to the reactants, characterizing the reaction as endothermic. Meanwhile, in bottom picture of Figure 7, the reactants start from around 10 kcal/mol, surmount a barrier of about 6 kcal/mol, with the final product's free energy around 0 kcal/mol. Here, the energy of the products is lower than that of the reactants, indicating an exothermic reaction.

However, based on the Intrinsic Reaction Coordinate (IRC) analysis in the gas phase for both systems, the conclusion was that both are exothermic reactions. Clearly, the results shown in top picture of Figure 7 are anomalous. Consequently, we checked each window of the umbrella sampling process to pinpoint the cause of the aberrant results.

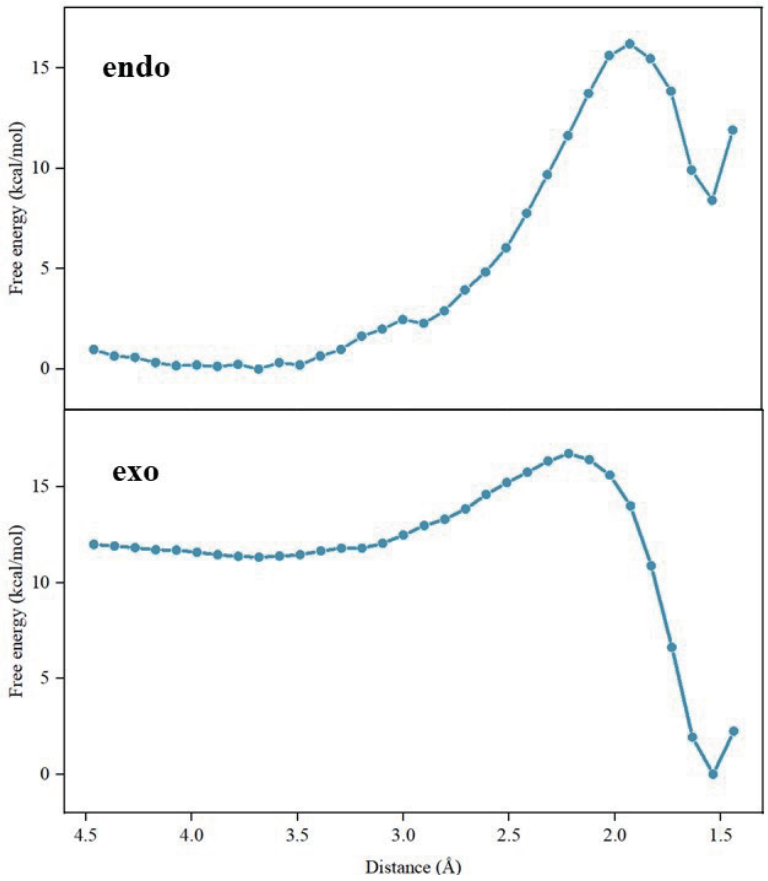

Figure 7. Free energy curve in a single reaction coordinate.

As illustrated in Figure 8, the sampling windows along the single reaction coordinate are shown, representing the reaction pathways for both the exo and endo addition systems. The red polyline represents the reaction path of the exo addition system, while the blue polyline represents that of the endo addition system. In the larger graph on the left, we can clearly observe that the umbrella sampling for each system is divided into two sections. The first section, from reactants to the transition state, spans from 1.4 Å to 1.9 Å for the endo addition system and from 1.4 Å to 2.2 Å for the exo addition system. The second section, from the transition state to the products, spans from 2.0 Å to 4.5 Å for the endo addition system and from 2.3 Å to 4.5 Å for the exo addition system.

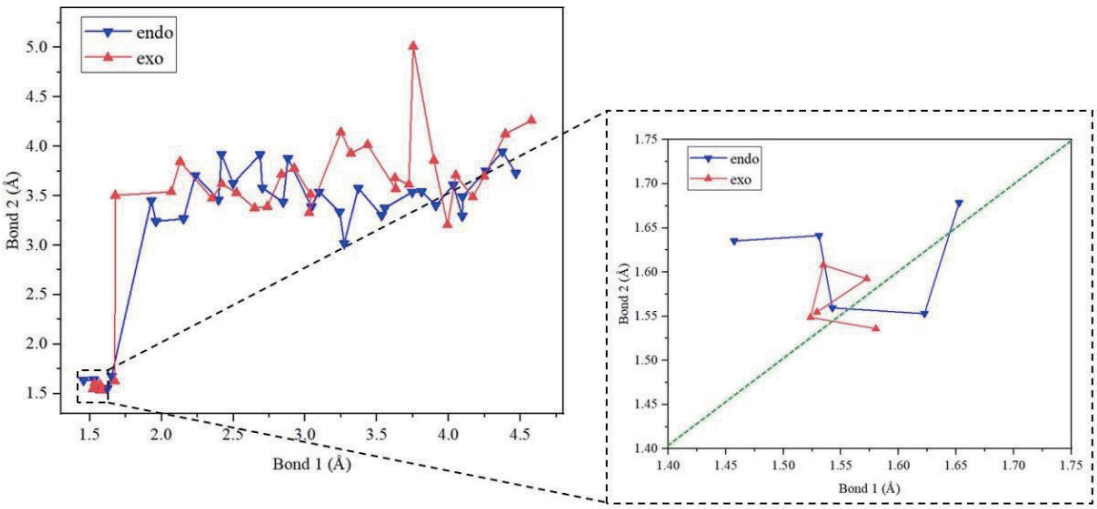

Figure 8. The reaction path shown by sampling window of endo and exo addition system in a single reaction coordinate system.

Analysis of the umbrella sampling protocol revealed limitations in using C4-C5 and C81-C83 bond lengths as a unified reaction coordinate for this asynchronous Diels-Alder system. While Bond 1 maintained proximity to constrained values in section II sampling, Bond 2 exhibited uncontrolled fluctuations due to lacking harmonic potentials. Critical examination of section I sampling windows (1.4-1.8 Å) demonstrated spontaneous Bond 1 formation (1.55-1.6 Å) despite stringent 400 kcal $mol^{-1}Å^{-2}$restraints, suggesting intrinsic reaction pathway preferences. Spatial analysis of bond length relationships (Figure 8) identified non-physical configurations where Bond 2 formed prior to Bond 1–a mechanistic inversion contradicting intrinsic reaction coordinate (IRC) predictions. These off-pathway conformations explain the elevated energies contributing to the endothermic profile in Figure 7.

To reconcile sampling artifacts with enzymatic reaction dynamics, we implemented a bifurcated protocol:

1. Bond formation phase: Bond 1 served as the primary coordinate with Bond 2 constrained (3.0-4.0 Å) to prevent premature formation (Table 2). Post-transition state windows maintained conventional sampling.

2. Bond stabilization phase: Bond 2 became the coordinate while fixing Bond 1 at 1.55 Å.This sequential constraint strategy generated continuous potential of mean force (PMF) profiles that better reflect the enzyme's natural asynchronous mechanism, eliminating energy artifacts from unphysical bond formation sequences.

	1.4 Å	1.5Å	1.6 Å	1.7 Å	1.8Å	1.9 Å	2.0 Å	2.1 Å
endo	3.0 Å	3.0 Å	-0.007	3.1 Å	3.2 Å	3.2 Å	/	/
exo	2.9 Å	2.9 Å	3.0 Å	0.369	3.1 Å	3.2 Å	3.3 Å	3.4 Å

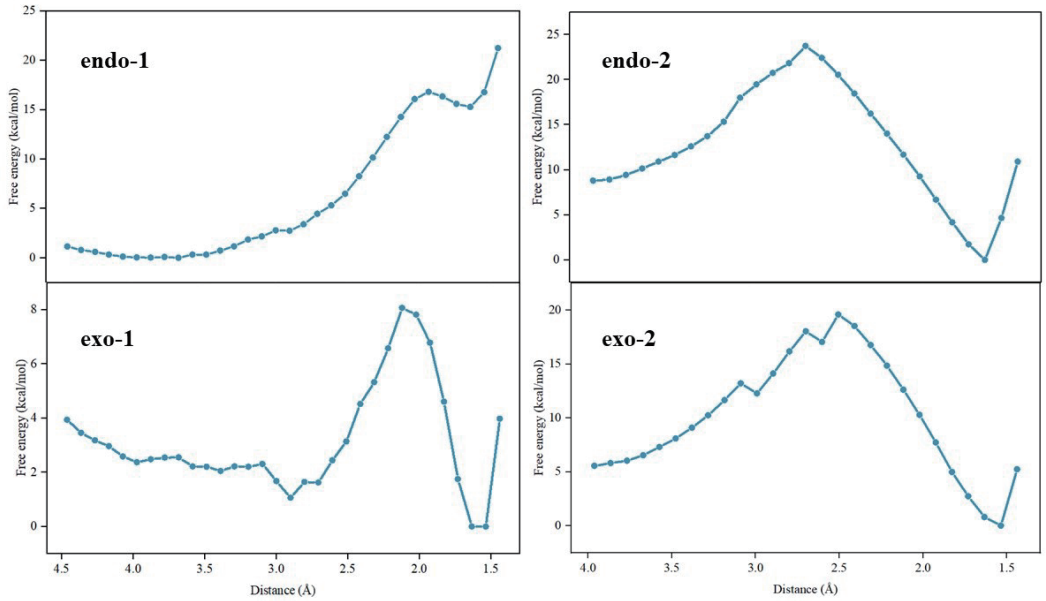

Figure 9. The reaction path shown by sampling window of endo and exo addition system in a double reaction coordinate system.

As depicted in top left picture of Figure 9, the PMF curve for the first part of the endo addition system's reaction shows that the reactants pass through a transition state to reach the 1.4 Å window. From there, sampling extends from the 3.0 Å window for Bond 2 in both directions, leading to the PMF curve of the second part of the reaction, shown in top right picture of Figure 9. In top right picture of Figure 9, an interesting phenomenon is observed: from the 3.0 Å window to the right, which corresponds to a decrease in Bond 2's length, the free energy initially rises and then declines; to the left, where Bond 2's length increases, the free energy continuously drops and stabilizes around the 3.9 Å window. This indicates the presence of two transition states and an intermediate in the reaction, suggesting an asynchronous mechanism for this Diels-Alder (DA) reaction. However, the IRC analysis in the gas phase indicated that the reaction follows a cooperative yet highly asynchronous mechanism. This likely signifies that the mechanism of the DA reaction changes from the gas phase to the enzyme environment.

A similar analysis was conducted for the exo addition system, as illustrated in bottom left picture of Figure 9. The reactants start from around the 3.0 Å window, go through a transition state, and finally reach the 1.4 Å window. Sampling then extends from the 3.0 Å window for Bond 2 in both directions, resulting in the PMF curve of the second part of the reaction shown in bottom right picture of Figure 9. We observe similar phenomena in the exo addition system, with two transition states present along the overall reaction pathway. This consistent finding across both systems highlights the complex, asynchronous nature of the DA reaction within the enzyme environment, differing from its behavior in simpler, non-enzymatic settings.

We then combined the free energy profiles of both systems and studied the overall properties of the reactions. As shown in Figure 10, the black line represents the overall reaction pathway and energy barriers for the endo addition system, while the red line represents those for the exo addition system. For the endo addition system, the reactants first pass through a transition state with an energy barrier of 16.8 kcal/mol, followed by the formation of a diradical intermediate. Then, they encounter another transition state with an energy barrier of 14.9 kcal/mol before finally forming the

endo addition product. For the exo addition system, the reactants first experience a transition state with an energy barrier of 7.0 kcal/mol, followed by the formation of a diradical intermediate. Subsequently, they pass through another transition state with an energy barrier of 13.7 kcal/mol before ultimately forming the exo addition product. At this point, we observed that the reactions in both systems are exothermic. We consider these results to be reasonable.

Additionally, for the endo-addition system, we utilized the same sampling method and obtained the corresponding PMF curves under the precision of GFN2-xTB[38] and SCC-DFTB[39] (Figure S3 to Figure S6). It was observed that, unlike with B3LYP, no radical intermediates were produced under these two methods. Therefore, we believe that semi-empirical approaches like GFN2-xTB and SCC-DFTB may not be suitable for studying the asynchronous mechanisms of Diels-Alder reactions.

Finally, we compared the reaction barriers in the enzyme with those in the gas phase. For the endo-addition system, the reaction barrier under enzyme catalysis was reduced by 6.4 kcal/mol compared to the gas phase. For the exo-addition system, the reaction barrier under enzyme catalysis was reduced by 4.3 kcal/mol. These computational results indeed indicate that Plol4 plays a catalytic role in the synthesis of Decatromicin.

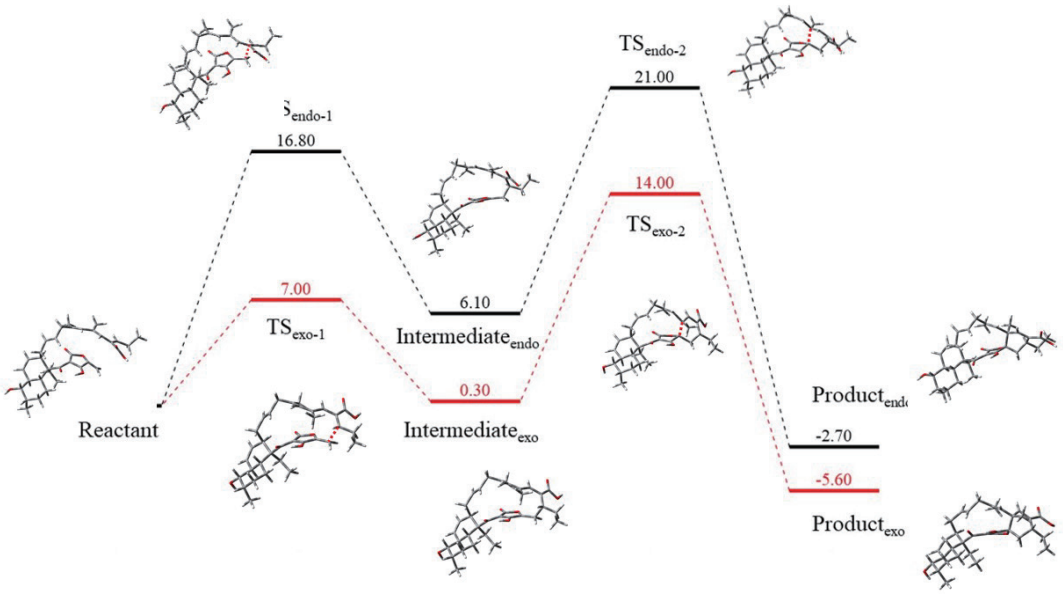

Figure 10. Overall reaction path and energy barrier of endo and exo addition system.

We subsequently analyzed the reasons for the mechanistic shift, using the endo addition system as an example. As shown in Figure 11, the left image displays the transition state structure of the endo addition system in the gas phase, while the right image shows a frame from the 1.9 Å window during sampling of the first part of the reaction in the enzyme (near the enzyme transition state structure). The two double bonds we are studying are marked with red circles. In the left image, the dihedral angle between the two double bonds is 18.6°, which is significantly different in the right image where the dihedral angle changes considerably from that in the gas phase.

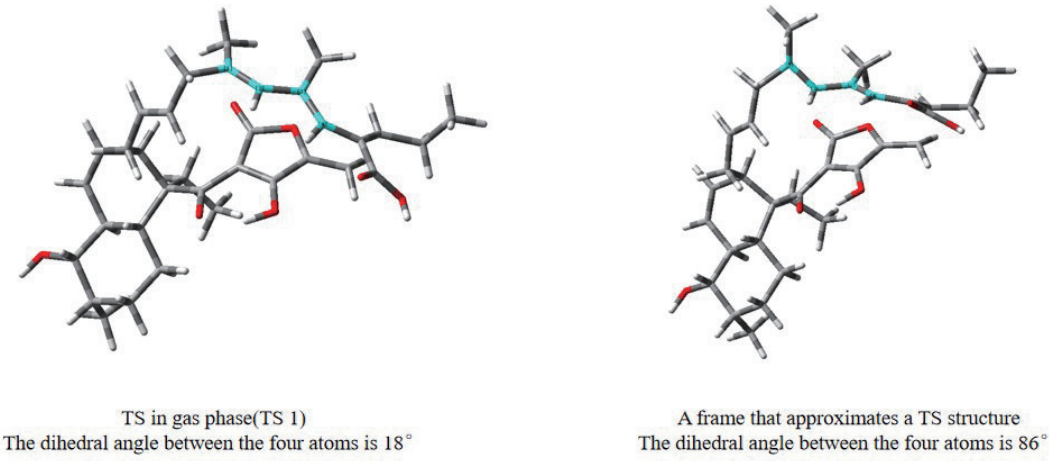

Figure 11. Transition state structure in endo addition system under two environments.

In Figure 12, we charted the changes in dihedral angles over the course of umbrella sampling for the endo addition system, represented by a blue line. Analysis reveals that during sampling, the dihedral angle swings widely, with most angles ranging between 50° and 100°, which is a significant deviation from the gas phase.

For the exo addition system, the dihedral angle between the same two double bonds is 24.5°. In Figure 12, a red line represents the changes in dihedral angle during sampling in the first part of the reaction at the 2.1 Å window. We observed that in the first half of the sampling, the dihedral angle fluctuates significantly, ranging from 0° to -50°, while in the latter half, it tends to stabilize between 20° and 30°. The first half shows a significant deviation from the gas phase, but the latter half is relatively stable.

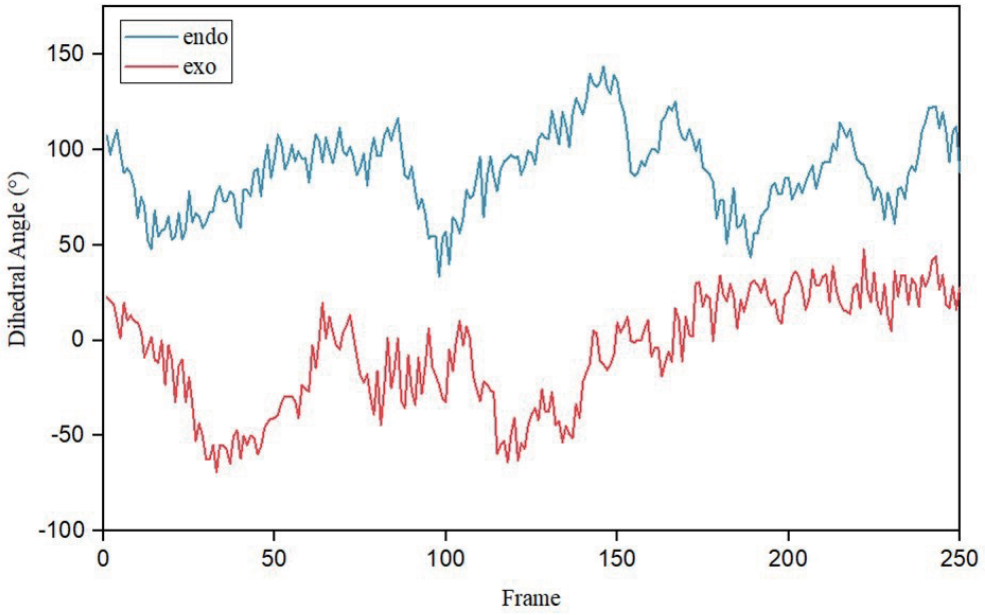

Figure 12. The dihedral angle of the window near the transition state varies with time in two addition systems.

In the gas phase transition states of both addition systems, the dihedral angles between the two double bonds are small, tending towards parallel alignment. This alignment allows for better π-orbital overlap and produces a π-π conjugation effect, which is not conducive to the formation of radical intermediates and favors a reaction mechanism that is cooperative yet highly asynchronous.

In the enzyme environment, for the endo system, the dihedral angle between the two double bonds is larger, approaching perpendicularity. This alignment almost eliminates π-orbital overlap, preventing the formation of π-π conjugation. However, if the reaction proceeds through an asynchronous mechanism, carbon atom C15 (located on one of the double bonds and also part of Bond 2) can become a radical intermediate in the reaction. This allows the formation of a σ-π hyperconjugation effect with the other double bond, thereby reducing the system's energy.

For the exo system, the dihedral angles at the early stages of sampling indeed differ significantly from those in the gas phase, while in the later stages of sampling, the angles do not differ significantly from those in the gas phase. This might be attributed to the short duration of the sampling, which could introduce some randomness. Considering the overall results from the PMF curves, this is considered reasonable. Therefore, the reasons for the mechanistic shift in the exo system are likely consistent with those observed in the endo system.

4. Conclusion

We explored the catalytic mechanism of the Plol4 enzyme in the synthesis of macrolide lactone antibiotics, employing a combination of quantum mechanics/molecular mechanics (QM/MM) methods, molecular dynamics (MD) simulations, and potential of mean force (PMF) simulations. Particularly, we made innovative improvements to the umbrella sampling method commonly used in Diels-Alder (DA) reaction studies. By implementing two harmonic potential constraints and dividing the reaction into two stages with distinct reaction coordinates, our method effectively handles DA reactions with asynchronous mechanisms and cooperative yet highly asynchronous mechanisms.Further analysis of the reaction pathways in both the gas phase and enzyme environments revealed a novel phenomenon: significant differences in the DA reaction mechanisms between the gas phase and the enzyme environment. While the gas phase exhibited a cooperative yet highly asynchronous mechanism, this shifted to an asynchronous mechanism within the enzyme environment. This shift is attributed to conformational changes in the substrate induced by the enzyme environment, thereby facilitating more effective formation of radical intermediates.

This discovery not only provides a new perspective on the catalytic mechanism of the Plol4 enzyme but also lays a theoretical foundation for the design of new antibiotics. This enhances our understanding of enzyme catalysis and opens new avenues for rational drug design targeting specific enzyme-mediated transformations.

Supporting information

The online version contains supplementary material available at website https://global-sci.com/storage/self-storage/cicc-2025-133-1-r1-si.pdf

Acknowledgments

This work was supported by the National Natural Science Foundation of China (Grant Nos. 22333006 and 92270001).

References

[1] Jeon B. S., Wang S. A., Ruszczycky M. W., Liu H. W. Natural [4+2]-cyclases. *Chem. Rev*., **117** (2017), 5367-5388.

[2] Jamieson C. S., Ohashi M., Liu F., Tang Y., Houk K. N. The expanding world of biosynthetic pericyclases: cooperation of experiment and theory for discovery. *Nat. Prod. Rep*., **36** (2019), 698-713.

[3] Zheng Q., Tian Z., Liu W. Recent advances in understanding the enzymatic reactions of [4+2] cycloaddition and spiroketalization. *Curr. Opin. Chem. Biol*., **31** (2016), 95-102.

[4] Kim H. J., Ruszczycky M. W., Choi S. H., Liu Y. N., Liu H. W. Enzyme-catalysed [4+2] cycloaddition is a key step in the biosynthesis of spinosyn A. *Nature*, **473** (2011), 109-112.

[5] Tian Z. et al. An enzymatic [4+2] cyclization cascade creates the pentacyclic core of pyrroindomycins. *Nat. Chem. Biol*., **11** (2015), 259-265.

[6] Hashimoto T. et al. Biosynthesis of versipelostatin: identification of an enzyme-catalyzed [4+2]-cycloaddition required for macrocyclization of spirotetronate-containing polyketides. *J. Am. Chem. Soc*., **137** (2015), 572-575.

[7] Byrne M. J. et al. The catalytic mechanism of a natural Diels–Alderase revealed in molecular detail. *J. Am. Chem. Soc*., **138** (2016), 6095-6098.

[8] Ohashi M. et al. SAM-dependent enzyme-catalysed pericyclic reactions in natural product biosynthesis. *Nature*, **549** (2017), 502-506.

[9] Zhang B. et al. Enzyme-catalysed [6+4] cycloadditions in the biosynthesis of natural products. *Nature*, **568** (2019), 122-126.

[10] Little R. et al. Unexpected enzyme-catalysed [4+2] cycloaddition and rearrangement in polyether antibiotic biosynthesis. *Nat. Catal*., **2** (2019), 1045-1054.

[11] Cai Y. et al. Structural basis for stereoselective dehydration and hydrogen-bonding catalysis by the SAM-dependent pericyclase LepI. *Nat. Chem*., **11** (2019), 812-820.

[12] Chen Q. et al. Enzymatic intermolecular hetero-Diels–Alder reaction in the biosynthesis of tropolonic sesquiterpenes. *J. Am. Chem. Soc*., **141** (2019), 14052-14056.

[13] Dan Q. et al. Fungal indole alkaloid biogenesis through evolution of a bifunctional reductase/Diels–Alderase. *Nat. Chem*., **11** (2019), 972-980.

[14] Gao L. et al. FAD-dependent enzyme-catalysed intermolecular [4+2] cycloaddition in natural product biosynthesis. *Nat. Chem*., **12** (2020), 620-628.

[15] Li Q. et al. Nonspecific heme-binding cyclase AbmU catalyzes [4+2] cycloaddition during neoabyssomicin biosynthesis. *ACS Omega*, **5** (2020), 20548-20557.

[16] Sato M. et al. Catalytic mechanism and endo-to-exo selectivity reversion of an octalin-forming natural Diels–Alderase. *Nat. Catal*., **4** (2021), 223-232.

[17] Zou Y., Houk K. N. et al. Computational investigation of the mechanism of Diels–Alderase PyrI4. *J. Am. Chem. Soc*., **142** (2020), 20232-20239.

[18] Li B., Houk K. N. et al. Mechanism of the stereoselective catalysis of Diels–Alderase PyrE3 involved in pyrroindomycin biosynthesis. *J. Am. Chem. Soc*., **144** (2022), 5099-5107.

[19] Wang H., Zou Y., Li M. et al. A cyclase that catalyses competing 2+2 and 4+2 cycloadditions. *Nat. Chem*., **15** (2023), 177-184.

[20] Walsh C. T. *Antibiotics: Actions, Origins, Resistance*. ASM Press, Washington, DC, 2003, p. 3.

[21] Frieri M., Kumar K., Boutin A. Antibiotic resistance. *Infect. Public Health*, **10** (2017), 369-378.

[22] Lagunin A. A., Goel R. K., Gawande D. Y. Chemo- and bioinformatics resources for in silico drug discovery from medicinal plants beyond their traditional use: a critical review. *Nat. Prod. Rep*., **31** (2014), 1585-1611.

[23] Tian Z., Sun P., Yan Y. An enzymatic [4+2] cyclization cascade creates the pentacyclic core of pyrroindomycins. *Nat. Chem. Biol*., **11** (2015), 259-265.

[24] Gerhard A., Muntwyler R., Keller-Schierlein W. Stoffwechselprodukte von Mikroorganismen: eine unerwartete Umwandlung in der Chlorothricin-Reihe. *Helv. Chim. Acta*, **58** (1975), 1323-1338.

[25] Muntwyler R., Keller-Schierlein W. Metabolic products of microorganisms: structure of the chlorothricins, a new macrolide antibiotic. *Helv. Chim. Acta*, **55** (1972), 2071-2094.

[26] Tamaoki T., Kasai M., Shirahata K. Tetrocarcins, novel antitumor antibiotics. II. Isolation, characterization and antitumor activity. *J. Antibiot*., **33** (1980), 946-950.

[27] Nakashima T., Miura M., Hara M. Tetrocarcin A inhibits mitochondrial functions of Bcl-2 and suppresses its anti-apoptotic activity. *Cancer Res*., **60** (2000), 1229-1235.

[28] Singh M. P., Petersen P. J., Jacobus N. V. Pyrroindomycins, novel antibiotics produced by Streptomyces rugosporus LL-42D005. II. Biological activities. *J. Antibiot*., **47** (1994), 1258-1265.

[29] Alksne L. E., Burgio P., Hu W. Identification and analysis of bacterial protein secretion inhibitors utilizing a SecA-LacZ reporter fusion system. *Antimicrob. Agents Chemother*., **44** (2000), 1418-1427.

[30] Zhu Y., Ouyang W., Wu N. Antibiotic resistance: sources and mitigation. *BCAS*, **30** (2015), 509-516.

[31] Ching K.-C., Chin E. J., Wibowo M., Tan Z. Y., Yang L.-K., Seow D. C., Leong C.-Y., Ng V. W., Ng S.-B., Kanagasundaram Y. Antibacterial spirotetronate polyketides from an *Actinomadura* sp. strain A30804. *Molecules*, **27** (2022), 8196.

[32] Frisch M. J. et al. *Gaussian 16, Version A.03*. Gaussian Inc., 2016.

[33] Grimme S., Antony J., Ehrlich S., Krieg H. A consistent and accurate ab initio parametrization of density functional dispersion correction (DFT-D) for the 94 elements H-Pu. *J. Chem. Phys*., **132** (2010), 154104.

[34] Becke A. D. Density-functional thermochemistry. III. The role of exact exchange. *J. Chem. Phys*., **98** (1993), 5648-5652.

[35] Trott O., Olson A. J. AutoDock Vina: improving the speed and accuracy of docking with a new scoring function, efficient optimization, and multithreading. *J. Comput. Chem*., **31** (2010), 455-461.

[36] Case D. A. et al. *Amber 20*. University of California, San Francisco, 2020.

[37] Grossfield A. WHAM: the weighted histogram analysis method, version 2.0.11. University of Rochester, 2018.

[38] Bannwarth C., Ehlert S., Grimme S. GFN2-xTB: an accurate and broadly parametrized self-consistent tight-binding quantum chemical method with multipole electrostatics and density-dependent dispersion contributions. *J. Chem. Theory Comput*., **15** (2019), 1652-1671.

[39] Rüger R., van Lenthe E., Lu Y., Frenzel J., Heine T., Visscher L. Efficient calculation of electronic absorption spectra by means of intensity-selected time-dependent density functional tight binding. *J. Chem. Theory Comput*., **11** (2015), 157-167.